

Instrumental chapters
COMPASS thesis

Armando Brandonisio

July 3, 2016

Contents

1	Absorber characterization	3
1.1	Absorber properties	3
1.2	Experimental set-up	5
1.3	Definition of the operative range	10
1.3.1	Set-up parameters	10
1.3.2	Expected efficiency	10
1.4	Circuit calibration with X-ray sources	11
1.4.1	Dark/Background noise	14
1.5	Energy resolution measurement	16
2	Scatterer characterization	17
2.1	Scatterer properties	17
2.1.1	Intrinsic properties	18
2.1.2	Coupling with SiPMs	20
2.2	Study of the dark current rate	21
2.2.1	Set-up parameters	21
2.2.2	Dark current comparison	22
2.3	Study of the light yield	27
2.3.1	Set-up parameters	27
2.3.2	Spectra analysis	27
	References	36



Chapter 1

Absorber characterization

Characterization of scintillator rods is a fundamental starting point to understand possibilities and limits of the entire experiment.

Absorber bars are the external objects of polarimeter design, and they must be made of a high atomic number Z to maximize the photoelectric absorption of the radiation and to minimize multiple scattering, which *destroys* the information on the polarization of the X-rays.

A good light yield and decay time ($\leq 1\mu s$) are required to optimize spectrum detection and coincidence measurements.

The agreement between the maximum of light emission spectrum and the photo-detection efficiency range of SiPM increases the collected charge of the readout process.

I characterized the scintillator rods by illuminating the scintillation rod with a X-ray beam.

I varied SiPM and electronic chain parameters and I measured the relative position of the photo-peak in the spectrum produced by the scintillator.

1.1 Absorber properties

I investigated luminescence and scintillation properties of the $Gd_3Al_2Ga_3O_{12} : Ce$ (GAGG) produced by Furukawa company.

The GAGG crystal has the highest light yield among oxide crystal at room temperature [1] and fast decay time for the detection of radioactivity and in nuclear and particle physics experiments.

A list of the most important parameters for GAGG is reported in Table 1.1.

Density [g/cm ³]	Light yield [photon/MeV]	Decay time [ns]	Peak emission [nm]	Energy resolution [% @662 keV]	Hygroscopicity
6.63	57000	88 (91%) 258 (9%)	520	5.2	No

Table 1.1: Physical and scintillation properties of GAGG (data from [2])

Some fundamental features of this crystal are that it has no intrinsic ra-

radioactivity and it is a non-hygroscopic material. This allows a better usage for experimentation with low risk of contamination from ambient.

I extracted from [3] the mass attenuation coefficient of GAGG for photoelectric absorption and Compton scattering (incoherent scattering in the figure). Results value in Fig 1.1.

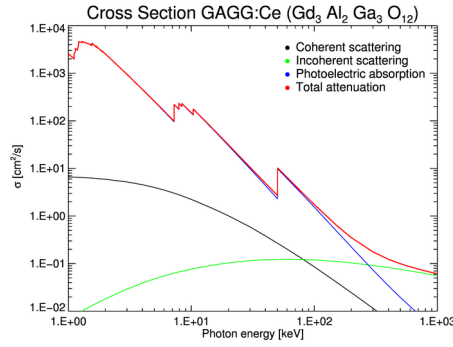


Figure 1.1: Mass attenuation coefficients for the GAGG crystal (Data from [3])

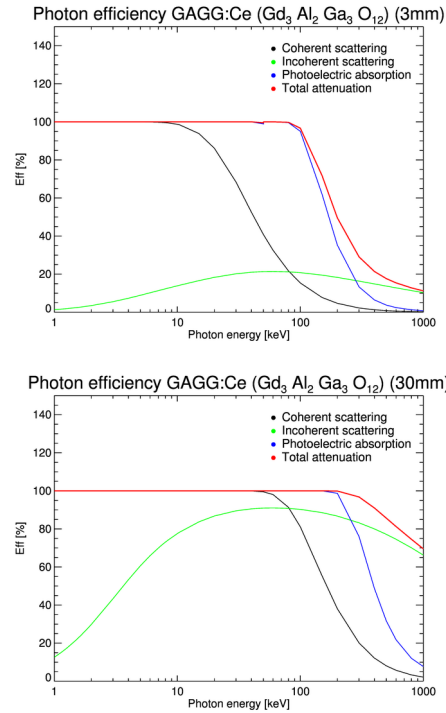


Figure 1.2: Total GAGG efficiency for a thickness of 3mm (left) and 30mm (right)

1.2 Experimental set-up

I used a single rod made of GAGG produced by *Furukawa* company.

The rod has the shape of a rectangular cuboid with square base of 3mmx3mm and height of 30 mm, thus their dimension results 2/3 lower to the one expected for the polarimeter bars ($\sim 10\text{mm}$).

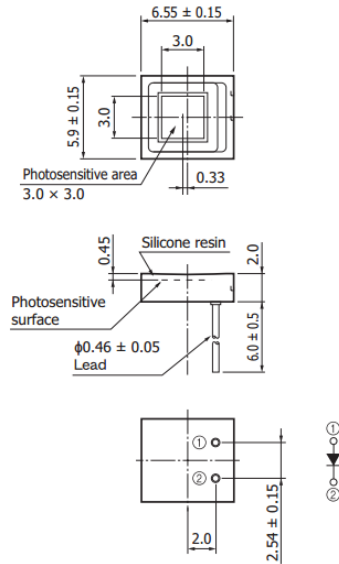
To minimize the loss of photons during scintillation, the bar was *wrapped* with Teflon tape Fig 1.3, that has a high light diffusion power.



Figure 1.3: Scintillation rod made of GAGG wrapped with teflon tape

I placed the rod on a single SiPM, models LCT4/9 and LCT5/1 produced by the Hamamatsu company.

Properties, CAD scheme and microscopic details of this SiPM are reported in Tab 1.2, Fig 1.4 and Fig 1.5 respectively.



LCT4/9

Cell pitch	$75\mu\text{m}$
Device size	$3 \times 3\text{mm}^2$
Microcells	1600
Surface coating	Silicone resin
Fill-factor	73%
Breakdown	51.10 V

LCT5/1

Cell pitch	$50\mu\text{m}$
Device size	$3 \times 3\text{mm}^2$
Microcells	3600
Surface coating	Silicone resin
Fill-factor	74%
Breakdown	52.5 V

Figure 1.4: CAD scheme for LCT4/9 and LCT5/1

Table 1.2: Main physical features of LCT/9 and LCT5/1

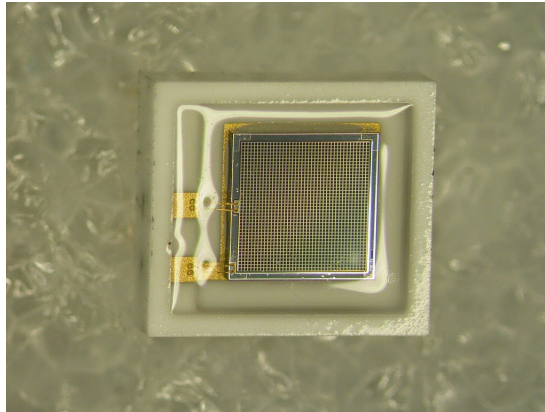


Figure 1.5: Image of LCT4/9 taken through a microscope.

This set of MPPCs produced by Hamamatsu, have an included proprietary circuit board with power supply for a direct hardware control from PC via USB connection (see Fig 1.6).

The C12332¹ is a simple evaluation starter kit for non-cooled MPPC. MPPC evaluation is possible by mounting an MPPC in the socket of the sensor circuit board. The power supply circuit board is equipped with the C11204-01, a high-accuracy, high-voltage power supply that provides the operating voltage from MPPC. It operates just by connecting to an external power supply ($\pm 5V$). It is also equipped with a USB interface that can be used to set the operating voltage and temperature compensation coefficient from a PC running the supplied sample software.

We used the power supply circuit board with serial number C12332 with nominal gain of 21 for LCT4/9.

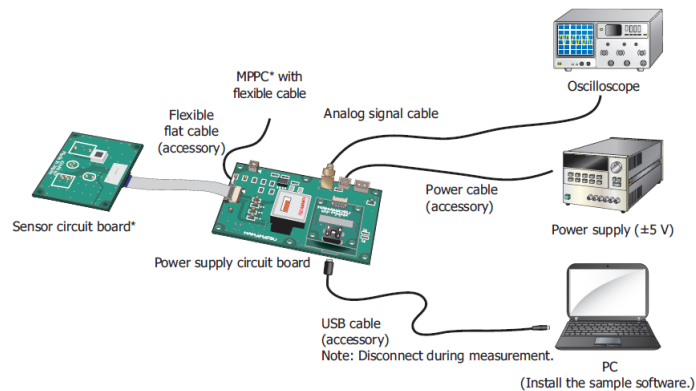


Figure 1.6: Connection example

¹Driver circuit for MPPC https://www.hamamatsu.com/resources/pdf/ssd/c12332-01_kacc1233e.pdf

I fixed both sensor circuit and power supply board both on an aluminum support covered by black duct tape (Fig 1.7).

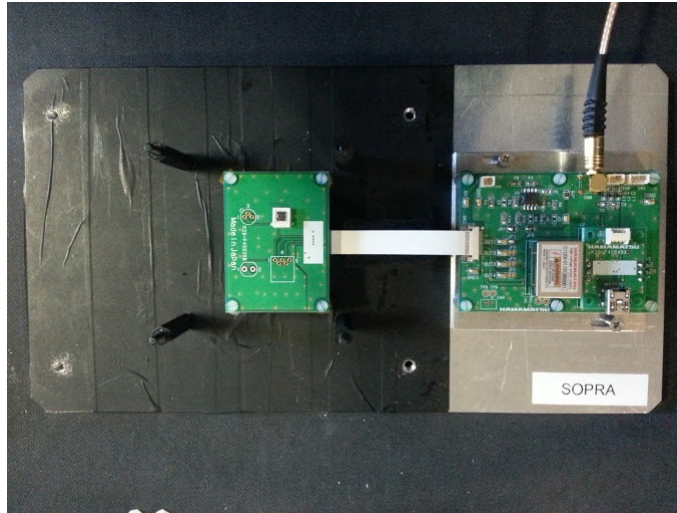


Figure 1.7: Circuit and sensor boards on support

I placed the GAGG rod on a single SiPM. I used optical grase for the optical contact between the GAGG rod and the window of the SiPM in order to improve the transmission of optical photons to the microcells.

A dedicated mechanical structure has been designed and produced specifically for this experiment in order to hold the rod under study and to guarantee its contact with the SiPM.

The project drawing is reported in Fig 1.8 and the principal components legend below:

- (1) Aluminum support
- (2) secondary mobile support for power supply circuit board
- (4) dark box
- (6-7) support columns
- (8) support for rod-stops
- (9) rod stops
- (11) circular support for x-ray sources

I show in Fig 1.9 a picture of the mechanical structure.

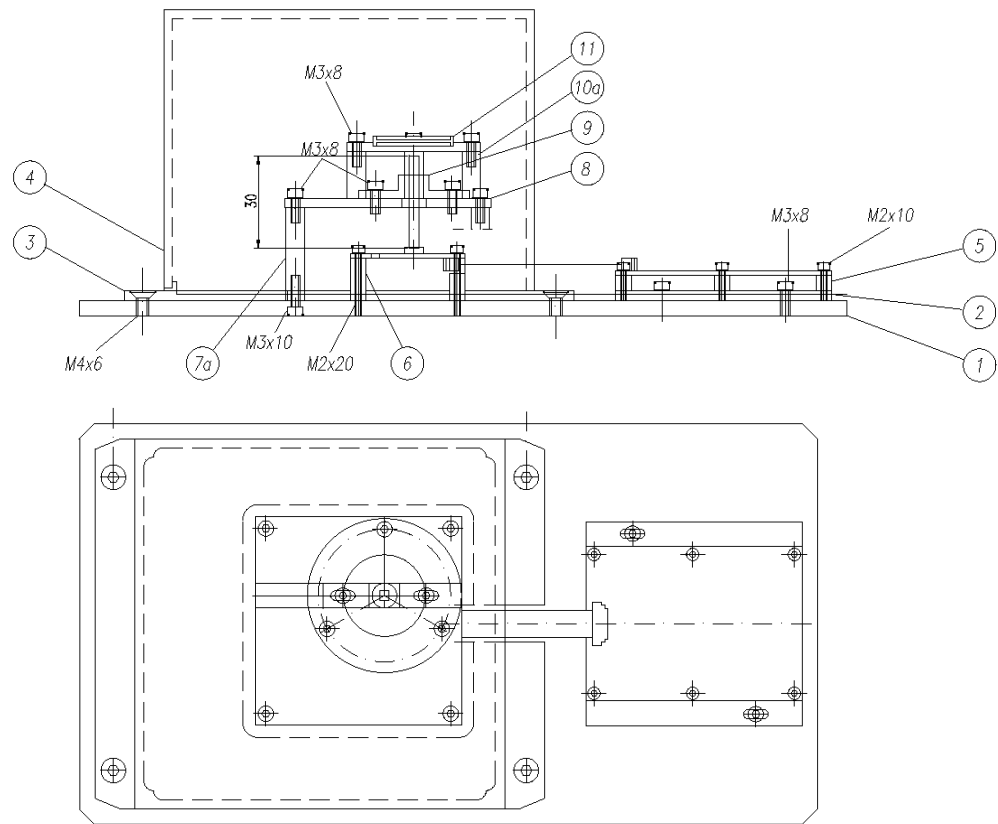


Figure 1.8: Front and side projection of entire setup.

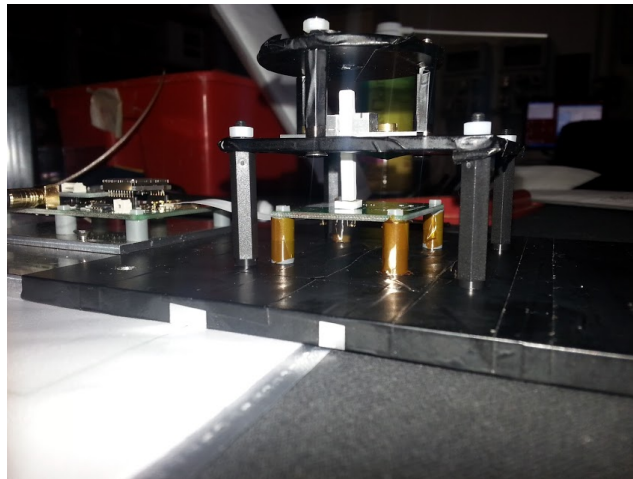


Figure 1.9: Built setup

I characterised the rod by illuminating with sources of ^{241}Am , ^{109}Cd , ^{133}Ba , ^{55}Fe , ^{137}Cs , placed at a distance of about 5mm from the rod top, put on a circular aluminum support designed for the used radioactive sources (Fig. 1.9). The source, produced by *Eckert & Ziegler* company, has a diameter of 3mm (Fig 1.10). It's flux has not been collimated.

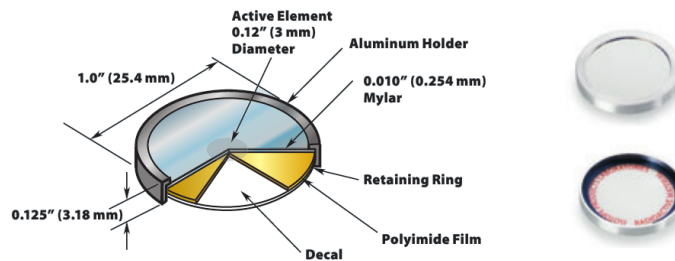


Figure 1.10: Type M disk used as x-rays source [4].

The alignment of the source along Z-direction has been carried out optically because the diameter of the beam spot was larger than the rod one, and therefore a rough alignment was sufficient.

I connected the output signal from the C12332 board (SMB connector) to an electronic chain composed of 'ORTEC 474 Timing filter Amplifier' or 'ORTEC 450 Research amplifier' and 'Amptek MCA8000A Multichannel Analyzer'. Electronic chain diagram is reported in Fig 1.11. Power supply circuit board allows to vary the operative voltage applied to the SiPM through USB connection and thus the SiPM internal gain.

The signal from SiPM was processed by a pre-amplifier welded on Hamamatsu circuit board and an amplifier ORTEC 450 *Research Amplifier*, and then digitized by a Multi-Channel Analyzer (MCA) Amptek 8000A, which splits signal into 1024 digital channels in a dynamic range of 0-5V or 0-10V.

The SiPM is very sensitive to visible light, therefore dark conditions are needed to perform the measurements. The dark conditions were assured by a *dark box* ((4) in Fig 1.8), a carton and a black cloth placed over the set-up.

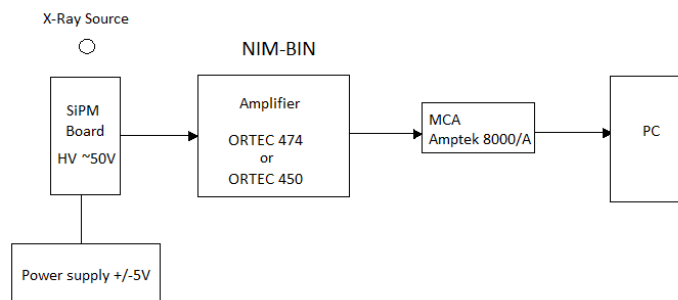


Figure 1.11: Sketch scheme of the electronic chain employed in the measurements to read and store SiPM signals

1.3 Definition of the operative range

1.3.1 Set-up parameters

Some preliminary operations must be performed before starting the measurement process. In particular, the parameters of the electronic chain must be set to proper values, the digital channels of the MCA must be converted into charge values through a calibration and the experimental conditions must be analyzed.

The gains of the used SiPM and amplifier can be varied. It has been necessary to properly set these parameters in order to generate a signal within a range suitable to the MCA input dynamics.

During the adjusting process, ~~the gains were changed~~ until the whole signal from the SiPM has been included in the spectrum collected by the MCA. An intense light source was necessary to guarantee a high measurement rate in order to collect a suitable number of events in a short time and to dominate dark current.

Here the instruments limitations:

- Following the Hamamatsu datasheet, the SiPM is not linear if $> 40\% - 50\%$ are simultaneously illuminated.
- MPPC signals are very fast ($< 100ns$) and very frequents, but MCA accepts a minimum shaping time of $250ns$ with a 'first peak detection'.

In order to prevent saturations or non-linearity in the final spectrum, we chose set-up parameters so that ^{241}Am photo-peak @ $59.5keV$ was placed in the middle of MCA dynamic range.

I know that our GAGG rod has a light yield of ~ 60 photons/keV [2] and the activity of the ^{241}Am is $\sim 10\mu Ci$.

I changed gain and integration time of ORTEC450 and *operative voltage* (V_{op}) of SiPMs to reduce possibility of spectrum distortion due to wrong shaping time or excessive gain.



1.3.2 Expected efficiency

To define an energy range of measurement system we needed to know maximum efficiency interval for scintillator rod, SiPMs and both. Detector efficiency, as function of energy, is defined by:

$$\epsilon(E) = T(E) \cdot A(E) \quad (1.1)$$

where $T(E)$ and $A(E)$ are respectively (1.2) transparency (1.3) and absorption with respect to energy radiation.

$$T(E) = e^{-\rho\delta\sigma(E)} \quad (1.2)$$

$$A(E) = 1 - e^{-\rho\delta\sigma(E)} \quad (1.3)$$

ρ is the material density, δ the thickness and $\sigma(E)$ the cross section sums for coherent/incoherent Compton scattering and photoelectric effect as a function

of energy. Plotted results are showed in Fig 1.2.

From literature I have found the SiPMs quantum efficiency curve [5] and the GAGG light emission [6] to calculate the total efficiency of SiPM+GAGG system (Eq 1.4).

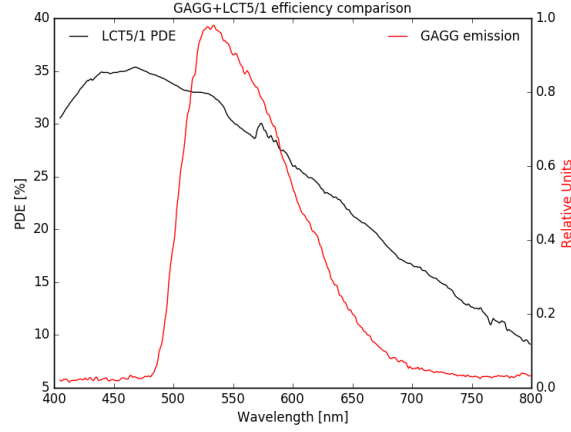


Figure 1.12: LCT5/1 QE and GAGG light emission

$$\epsilon_{tot} = \frac{\int_{\lambda} d\lambda \epsilon_{SiPM} \cdot \epsilon_{GAGG}}{\int_{\lambda} d\lambda \epsilon_{GAGG}} \quad (1.4)$$

Calculated efficiencies for LCT4/9 and LCT5/1 are listed in Tab 2.1.2.

SiPM	Tot. efficiency
LCT4/9 + GAGG	30.1%
LCT5/1 + GAGG	28.7%

Table 1.3: SiPM+GAGG efficiency

1.4 Circuit calibration with X-ray sources

I calibrated the electronic chain in order to convert the digital channels of the MCA output spectra in charge values. In the calibration I produced signals with similar amplitude, rise time and fall time of SiPM was produced by a pulse generator (BNC BL-2). I measured the values of applied voltages through an oscilloscope connected to circuit. At the same time, the channel number of the peak produced by the signal in the MCA spectrum was stored and associated with the applied voltage.

I calculated signal positions by weighted average for each amplitude value; example in Fig 1.13. This operation has been repeated for different V_{op} (Fig 1.14). Furthermore I performed spectra measurements with radioactive sources described in section 1.1 (Fig 1.15).

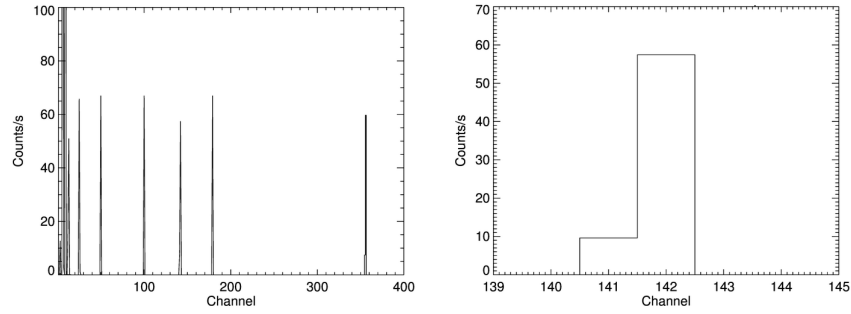


Figure 1.13: *Left figure:* Whole spectrum used for calibration. *Right figure:* Single signal acquired by MCA.

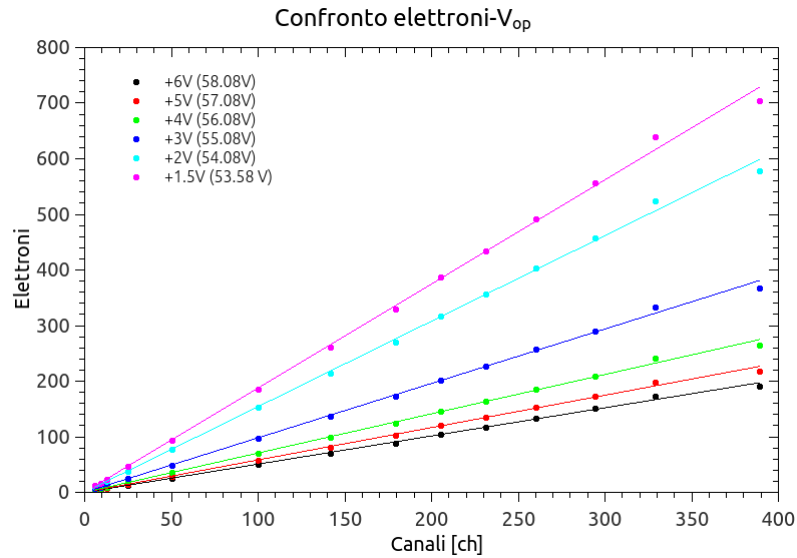


Figure 1.14: Linear calibration function used to convert the measured digital channels into charge values for LCT5/1.



I selected a gaussian model to fit sources photo-peaks. In order to improve fit, I studied a model that explain photopeak asymmetries for ^{109}Cd and ^{133}Ba (Fig 1.16). Nearest spectral lines are not resolved due to the low process resolution, then I assumed that the convolved lines have the same width (or resolution). The sum of all gaussian-like lines is the expected photopeak.

I associated experimental peak positions with well known laboratory sources spectra, then I calibrated MCA channels as a function of Energy (Fig 1.17). We also detected non-linearity for high energies values as expected (Fig 1.18).

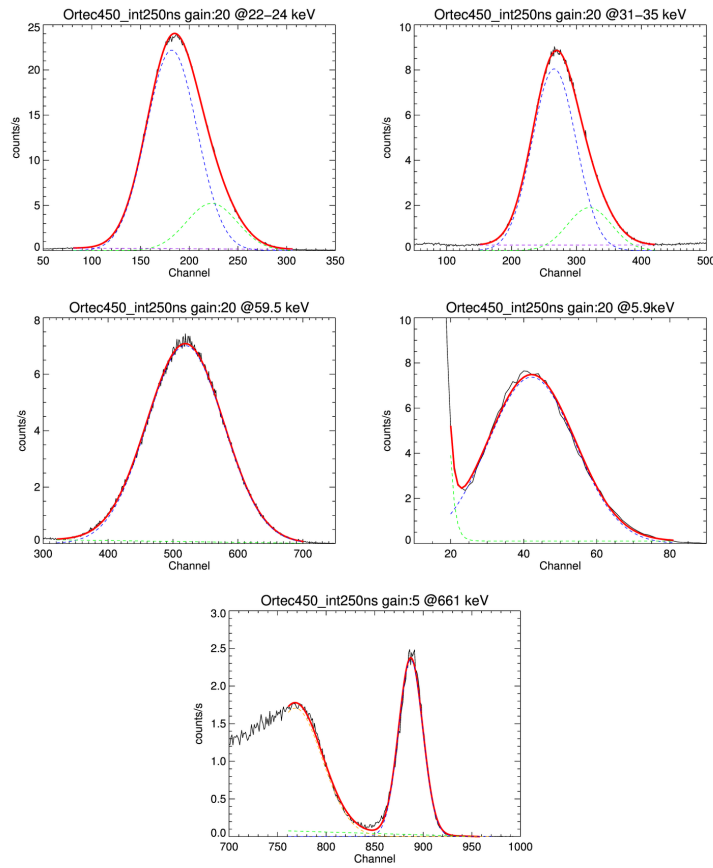


Figure 1.15: To left to right respectively: ^{109}Cd @ 22keV, ^{133}Ba @ 31keV, ^{241}Am @ 59.5keV, ^{55}Fe @ 5.9 keV, ^{137}Cs @ 661 keV

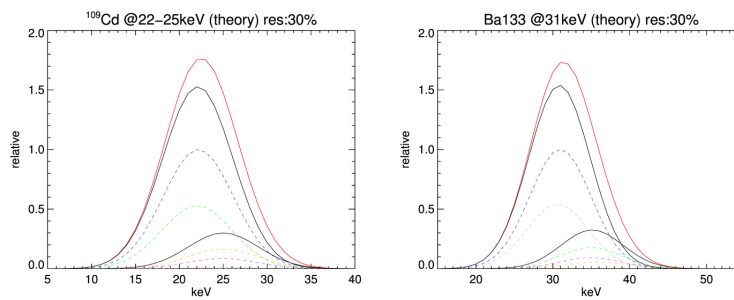


Figure 1.16: Theoretical model that assumes laboratory probability of each convoluted line for a resolution of 30%. Data from XCOM.

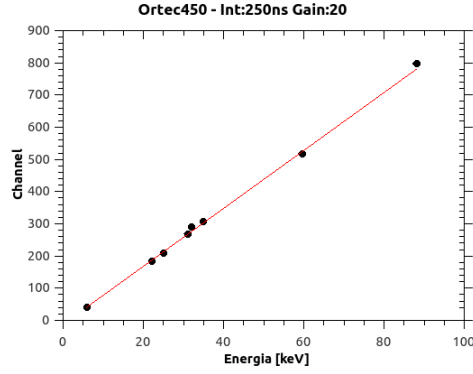


Figure 1.17: Linear energy calibration in the range of 0-90KeV for LCT4/9.

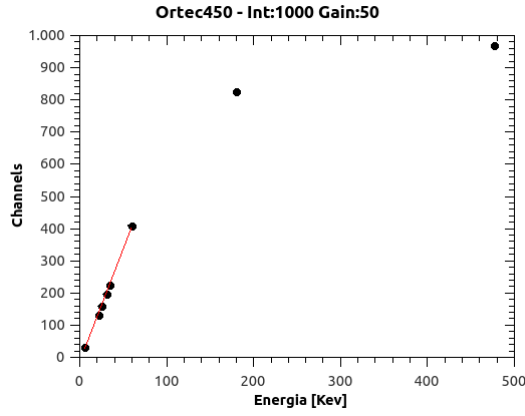


Figure 1.18: Non-linearity detection at high energies with LCT4/9.

1.4.1 Dark/Background noise

Dark current noise and environmental background spectra (Fig 1.19) are fundamental informations to select best configuration for acquiring data.

A study of *dark* counts has been performed to understand behavior of SiPM as V_{op} changes.

Environmental noise is negligible with respect to sources rate. At low charge collection dark current dominates.

An exponential curve was chosen to fit dark noise (Fig 1.20).

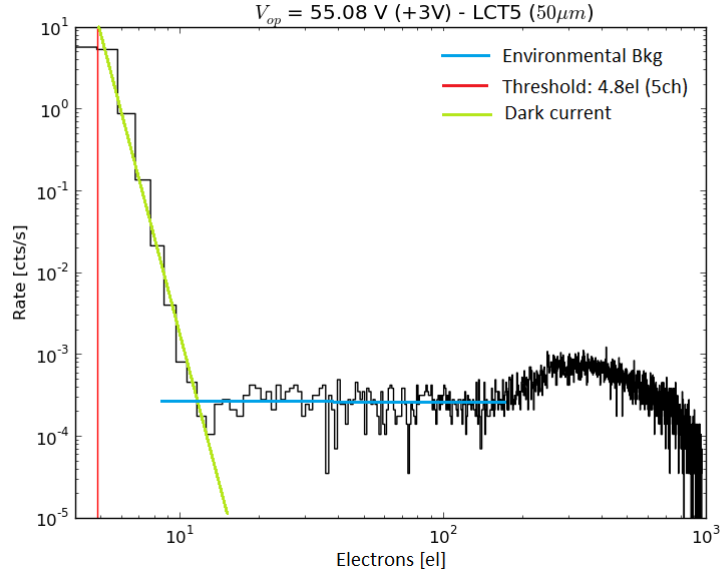


Figure 1.19: Dark current rate and environmental background acquisition with LCT5/1 ($V_{op} = +3V$) + GAGG.

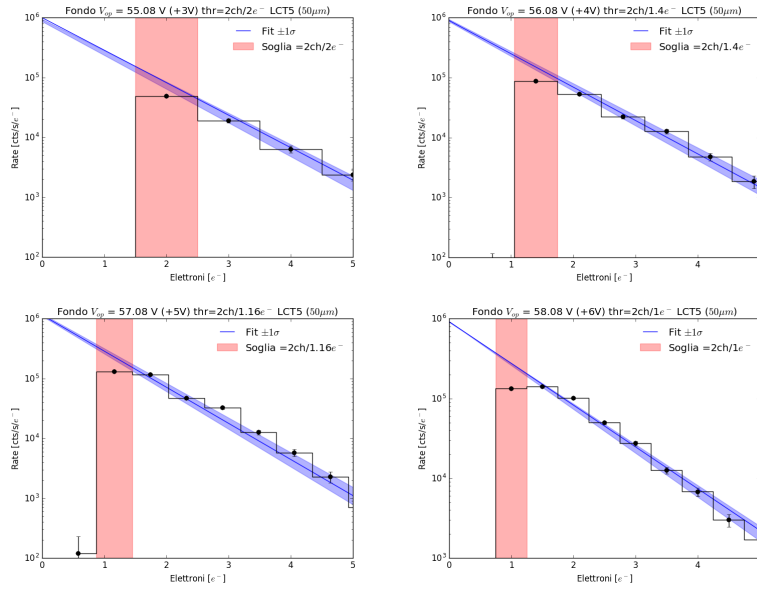


Figure 1.20: Dark rate study for LCT5/1 + GAGG

1.5 Energy resolution measurement

I analyzed fitted sources photopeaks of section 1.3 to study energy resolution as a function of V_{op} .

We note that dark rate increases with the increase of V_{op} but resolution seems to be better (decreases) with V_{op} .

Left plot of Fig 1.21 (^{55}Fe @ 5.9 keV), has an irregular distribution with respect to ^{241}Am case, due to nearness of dark noise that affects error of photopeak position and width.

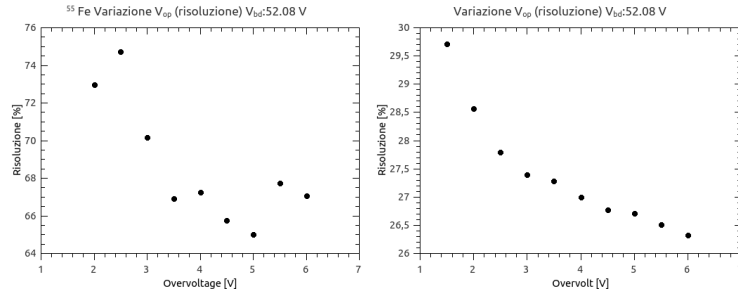


Figure 1.21: Resolution for ^{55}Fe peak (left) and (^{241}Am) peak as function of V_{op} .

Chapter 2

Scatterer characterization

Scatterer rods are the inner components of Compton polarimeter design. They are made of plastic scintillator and wrapped with Teflon tape.

Plastic scintillators have a low atomic number Z which maximize the probability for the incident radiation to undergo Compton scattering.

These kind of scintillators have a light yield ~ 3 -times lower than GAGG or high- Z materials, for this reason I needed to change circuit board parameters to increase nominal gain.

The measurement have been carried out by illuminating the scintillation rod with a X-ray source.

The high-gain system allows to show the SiPM quantized spectrum, that has been analyzed with a ad-hoc software (discussed in the next chapter) to extract physical informations as resolution, calibration and collected charge.

2.1 Scatterer properties

I investigated luminescence and scintillation properties of plastic rods produced by *Eljen Technology*, listed in Tab 2.1.

Eljen Technology's plastic scintillators are based on a plastic matrix of polyvinyl-toluene ($C_{27}H_{30}$) and fluors necessary to give each plastic scintillator its unique properties:

- **EJ-200:** combines the two important properties of long optical attenuation length and fast timing which make it particularly useful for time-of-flight systems using scintillators greater than one meter long. It is the detector of choice for many industrial applications, such as gauging and environmental protection, where high sensitivity and signal uniformity are critical operating requirements. [7]
- **EJ-204:** has the highest scintillation efficiency of any of Eljen's plastic scintillators, along with the combination of high speed and good attenuation length. It is particularly well suited for high-performance detector systems for nuclear and high-energy physics research. Its emission wavelength near 400 nm couples ideally with bi-alkali phototubes while still being long enough to be effectively used with UVT light guides. [7]

- **EJ-260:** is a green emitting plastic scintillator that has been formulated for use where longer wavelengths are advantageous for purposes of light piping. The green fluorescence is of short enough wavelength and the scintillation efficiency is high enough for successful use with conventional blue sensitive photomultiplier tubes. [8]

EJ-200 and EJ-204 have the properties of long optical attenuation length and fast timing with an emission spectrum well matched to common photomultipliers.

EJ-260 and green emitting plastic scintillators have been formulated for use where longer wavelengths are needed for efficient optical coupling to solid-state photosensors. Because of their longer emission wavelengths, they will exhibit somewhat greater radiation hardness than conventional blue plastic scintillators.

PROPERTIES	EJ-200	EJ-204	EJ-260
Light Output (% Anthracene)	64	68	60
Scintillation Efficiency (photons/1Mev e^-)	10000	10400	9200
Wavelength of Maximum Emission [nm]	425	408	490
Light Attenuation Length [cm]	380	160	350
Rise Time [ns]	0.9	0.7	1.3
Decay Time [ns]	2.1	1.8	9.2
Pulse Width, FWHM [ns]	2.5	2.2	-
H Atoms per cm^3 ($\cdot 10^{22}$)	5.17	5.15	5.21
C Atoms per cm^3 ($\cdot 10^{22}$)	4.69	4.68	4.70
Electrons per cm^3 ($\cdot 10^{23}$)	3.33	3.33	3.35
Density [g/cm ³]	1.023	1.023	1.023
Polymer Base	Polyvinyltoluene		
Refractive Index	1.58		
Softening Point	75°C		
Vapor Pressure	Vacuum-compatible		
Coefficient of linear expansion	$7.8 \cdot 10^{-5}$ below 65°C		
Temperature Range	-20°C to 60°C		
Light Output vs. Temperature	At 60°C, L.O.=95% of that at 25°C. No change from -60°C to 20°C		

Table 2.1: Scatterer rods properties from [7] [8].

2.1.1 Intrinsic properties

All Eljen plastic scintillator rods are made of Polyvinyltoluene ($C_{27}H_{30}$), and small internal variations between EJ-200, EJ-204 and EJ-260 are negligible to study interaction with X-ray photons.

In Tab 2.1 are listed all basic features of used plastic scintillators, so I calculated mass attenuation coefficient with respect to photon energy between 1keV and 100 keV (Fig 2.1).

In the energy range of 1keV-10keV the photoelectric effect dominates. When energy photons is ~ 20 keV, the mass attenuation coefficients of photoelectric

effect and Compton effect are almost the same, and for energy between 20keV and 100keV Compton effect dominates.

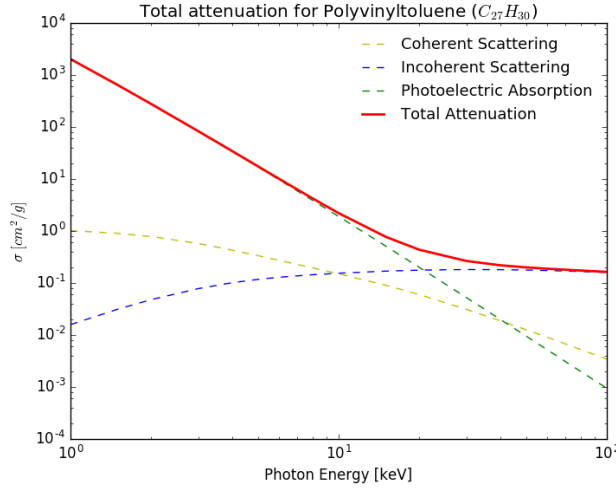


Figure 2.1: Mass attenuation coefficient for Eljen plastic scintillators. (Data from [3])

From equations (1.3) I calculated efficiency of total interactions for a 60mm thick rod (Fig 2.2).

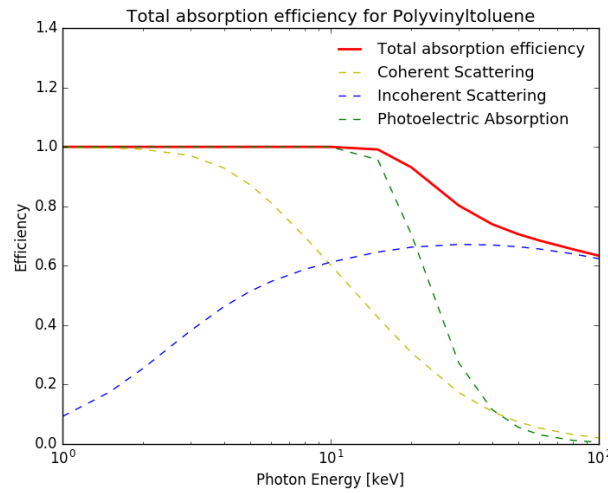


Figure 2.2: Total Polyvinyltoluene absorption efficiency for a thickness of 60mm

2.1.2 Coupling with SiPMs

I Placed The Eljen rods over a single SiPM. The extremity of the rod in contact with the SiPM window entrance has been covered with optical grease in order to improve the transmission of optical photons to the microcells.

Used scatterers have different emission spectra (Fig 2.3) and this makes different ways to optimize system efficiency when coupling with different SiPMs.

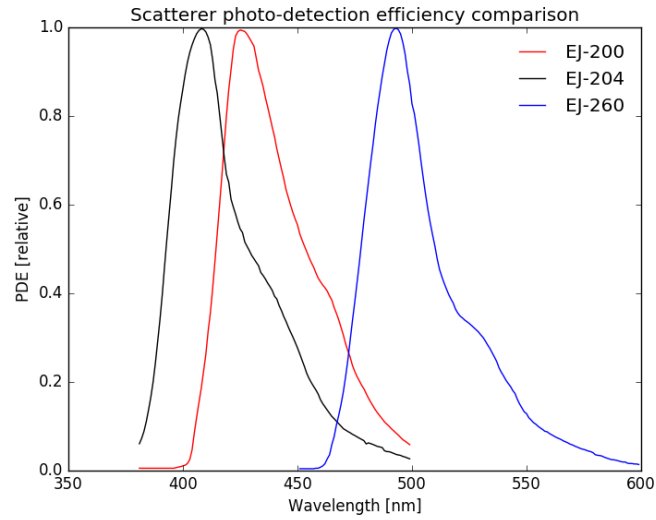


Figure 2.3: Emission spectrum of EJ-200 [9], EJ-204 [10], EJ-260 [11]

Used SiPM has been studied by Bonanno et al. [12] that measured their photon detection efficiency (PDE) (Discussed in [Capitolo sui SiPM](#)). I combined SiPMs PDE and scatterers emission spectra (Fig 2.4) to calculate total efficiency of a single rod case.

In the ideal case, the overall system efficiency is:

$$\varepsilon_{tot} = \varepsilon_{SiPM} \cdot \varepsilon_{scatt} \cdot \varepsilon_{geom} \quad (2.1)$$

where ε_{SiPM} is the SiPM PDE, ε_{scatt} is the scintillator efficiency and ε_{geom} is the fraction of max light yield due to rod geometrical shape.

In realistic case I must add another term ε^* into equation 2.1 because there are additional factors that decrease overall efficiency, like light loss through the rod and imperfect coupling between scatterer and SiPM with optical grease, causing a further loss of light. So equation 1.3 becomes:

$$\varepsilon_{tot} = \varepsilon_{SiPM} \cdot \varepsilon_{scatt} \cdot \varepsilon_{geom} \cdot \varepsilon^* \quad (2.2)$$

All Eljen tested scintillators are made of the same polymer, so I can assume that $\varepsilon_{geom} \cdot \varepsilon^*$ is the same for all scatterer rods ([probabilmente no, da rivedere](#)). For this reason I compared overall efficiencies normalized to $\varepsilon_{geom} \cdot \varepsilon^*$ using 1.4. Results in Tab 2.1.2.

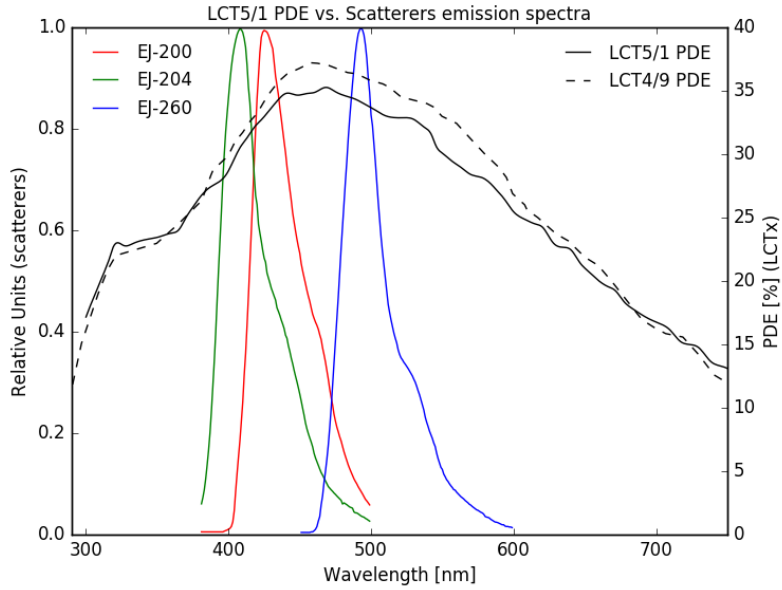


Figure 2.4: Comparison between SiPMs photon detection efficiency and scatterers emission spectra

	LCT5/1	LCT4/9
Config.	Tot. Efficiency	Tot. Efficiency
EJ-200	33.7%	35.2%
EJ-204	31.5%	32.7%
EJ-260	32.7%	35.5%

Table 2.2: Overall efficiencies for SiPMs + scatterers system normalized to $\varepsilon_{geom} \cdot \varepsilon^*$.

2.2 Study of the dark current rate

The first step of scatterer characterization is to choose SiPM with lower dark rate and better single photon resolution.

I tested and compared three types of SiPMs as a function of the overvoltage applied to the SiPM.

2.2.1 Set-up parameters

Eljen plastic scintillators have a light yield of ~ 10 ph/keV, ~ 3 -times lower than GAGG, as discussed at the beginning of chapter. Therefore I needed to

use a circuit board with preamplifier gain of 100. Used power supply circuit board was C12332 produced by Hamamatsu: the same tested for GAGG rod, but with an increased gain for preamplifier.

The experimental set-up was the same used for GAGG measurements (Fig 1.8) and the electronic chain is reported in Fig 2.5.

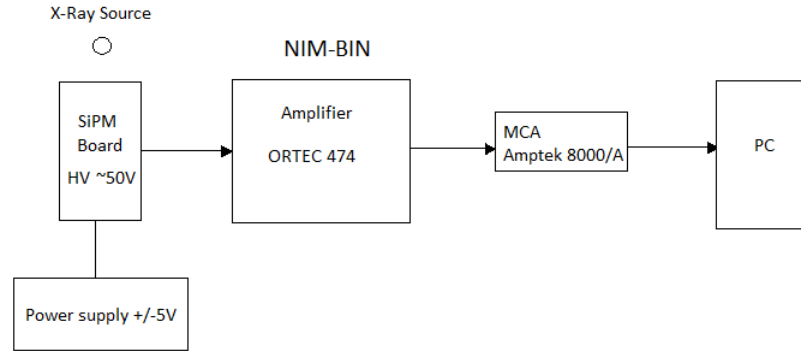


Figure 2.5: Sketch scheme of electronic chain employed in the measurements to read and store SiPMs+scatterers signals.

I chose the following parameters to perform measurements:

- Amplifier configuration (Ortec 474):
 - Coarse gain: 10
 - Fine gain: 2
 - Integration time: 50 ns
 - Differentiation: OUT
- MCA 8000A configuration:
 - dynamic range: 0-5 V
 - ADC channels: 4096

2.2.2 Dark current comparison

The aim of dark noise study is to choose the SiPM with better performances. The way is to find a well defined single photon spectrum with lowest counting rate at the same set-up conditions.

I studied dark current of LCT5/1 ($50\mu m$), LCT4/9 ($75\mu m$) and LCT4/20 ($100\mu m$). LCT5 SiPMs, as discussed in (capitolo sipm), are new generation photomultipliers compared to LCT4 sensors, with sensitive reduction of afterpulses and crosstalk effects.

I measured and compared SiPMs spectra changing nominal overvoltage parameter.

I first studied considered SiPMs at nominal voltage (+3V) (Fig 2.6).

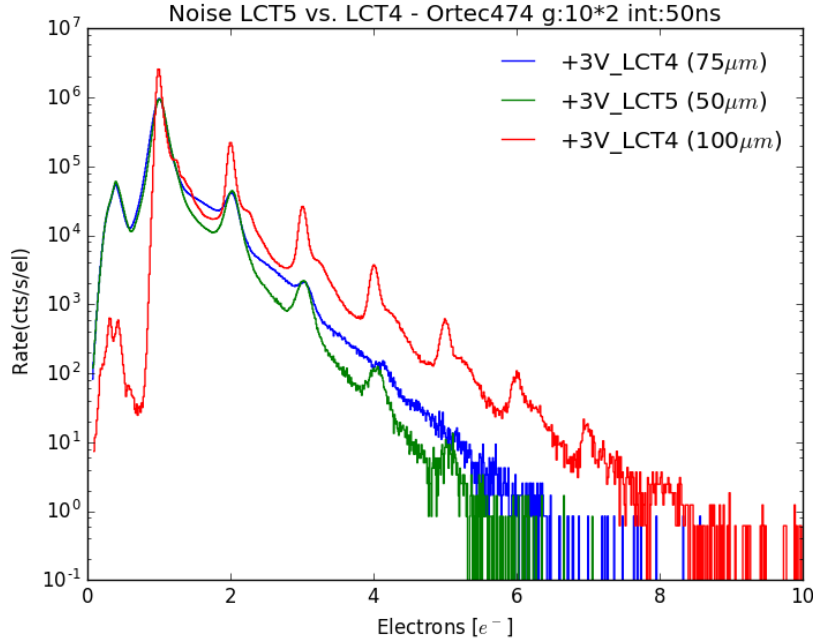


Figure 2.6: Dark rate comparison at nominal overvoltage for LCT5/1, LC4/9 and LCT4/20.

LCT5/1 and LCT4/9 have a comparable single photon rate, but the first one has a lower rate between single PE signals that allows to distinguish all single photon spectra.

LCT4/20 has a good single photon resolution but higher counting rate compared to other SiPMs. Furthermore this sensor achieves an higher collected charge value ($\sim 9e^-$) compared to others photomultipliers ($\sim 6e^-$) and this affects signal to noise ratio.

I performed other measurements to varying of overvoltage between +2V and +5V:

- LCT5/1:

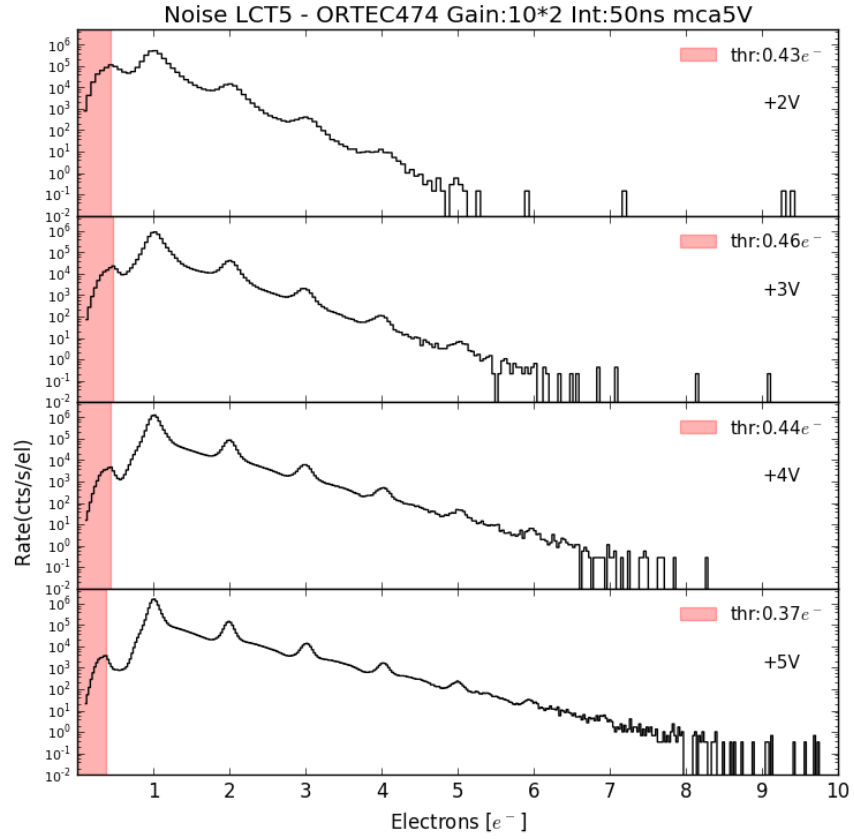


Figure 2.7: Dark rate comparison changing overvoltage for LCT5/1.

In order to compare dark noise rate I chose an interval between 1-PE and 4-PE weighted position. Then I integrated the same charge range for all overvoltage values to study noise total counts (Fig 2.8). Results are showed in Fig 2.9.

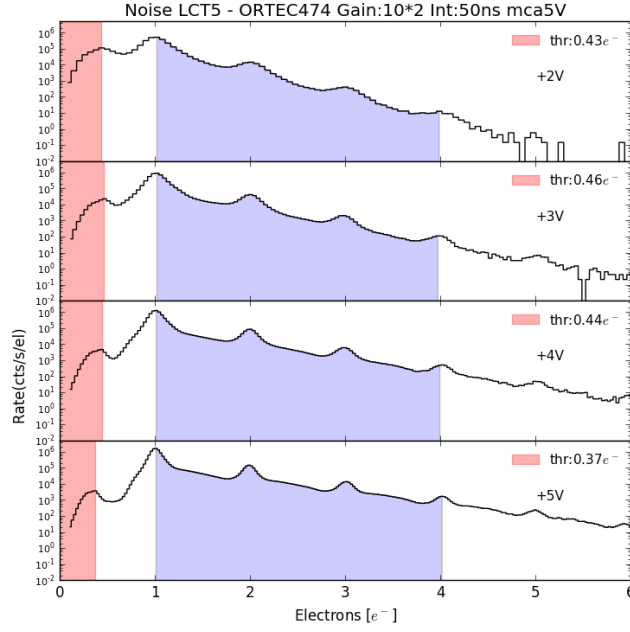
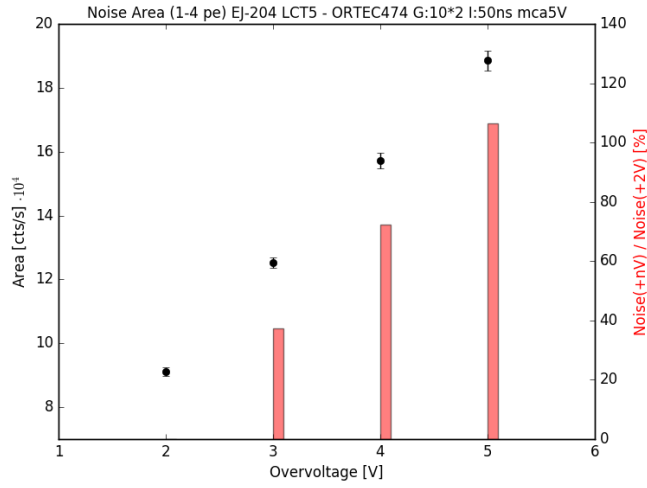


Figure 2.8: Noise integration between 1-4 PE for LCT5/1.

Figure 2.9: Integration results between 1-4 PE for LCT5/1. Black dots are the integrated area results, red bars are the percentage difference with respect to $V_{op} = +2V$ integrated area.

The result is that increasing of overvoltage affects noise total rate of ~ 2 times between +2V and +5V values (Fig 2.9).

- LCT4/9:

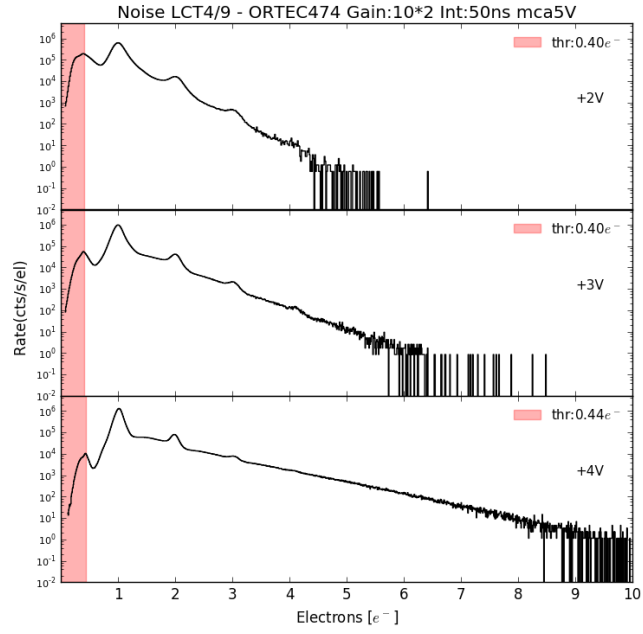


Figure 2.10: Dark rate comparison changing overvoltage for LCT4/9.

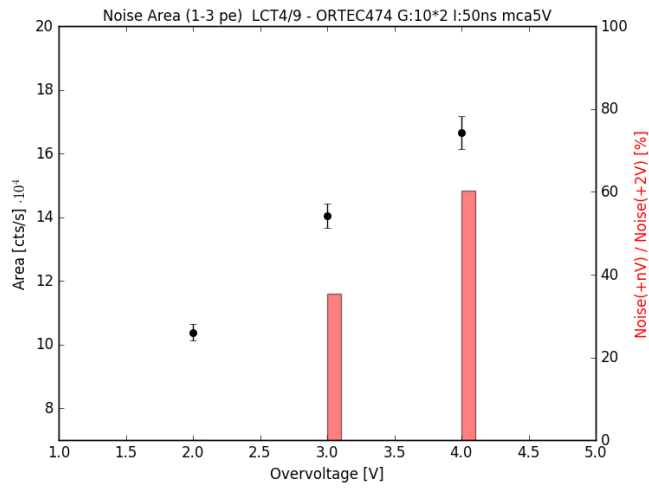


Figure 2.11: Integration results between 1-4 PE for LCT4/9.

Finally I chose LCT5/1 SiPM as sensor with lower dark current rate and better signal to noise ratio for high energy measurements.

2.3 Study of the light yield

The aim of scatterers characterization is to achieve the highest charge collection with best resolution of source photo-peak changing overvoltage value. After choosing SiPM with best performances, I coupled sensor with scintillators to perform measurements with X-ray source.

I used ^{109}Cd source to illuminate the rods. It's activity was $\sim 5.8\mu\text{Ci}(215\text{kBq})$ while acquiring data.

Used scintillators rods are EJ-200, EJ-204 and EJ-260, with a size of $3\times 3\times 60\text{mm}$.

2.3.1 Set-up parameters

The experimental set-up was the same described in Par 2.2.1, with one exception: coarse gain was 4 instead of 10.

In order to prevent saturation or non-linearity in the final spectrum, I chose this set-up parameters so ^{109}Cd photo peak @ 22 keV was placed in the $\sim 3/4$ of MCA dynamic range while overvoltage is +6V.

2.3.2 Spectra analysis

All spectra analysis was performed with following ad hoc python tasks (discussed in ...):

- `find_peak` : function that finds spectrum peaks
- `mg_fit` : multi-gaussian fit
- `fwhm_lin` : study of FWHM/\sqrt{N} linearity
- `cal_lin` : collected charge calibration
- `position_diff` : linearity of n-PE position
- `fit_area` : fitting integrated area or source photo-peak

An example of acquired spectrum with photo-peak is showed in Fig 2.12.

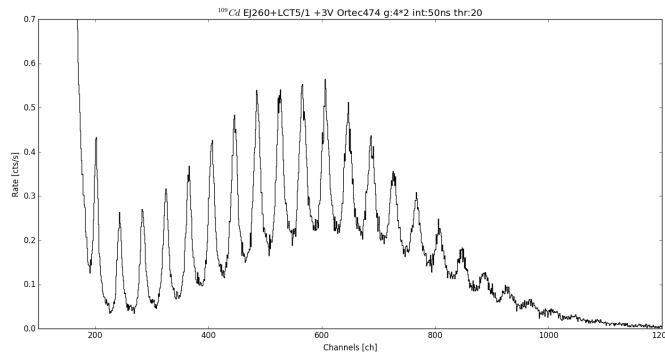


Figure 2.12: Acquired spectrum of ^{109}Cd @ 22keV with EJ-260+ LCT5/1 (+3V).

As discussed in (cap sipm), SiPMs spectra at high gain are composed of multiple gaussian peaks for single photo-electron (PE) value that are distributed according to Poisson probability.

Physical properties of photo-peak need to be extracted integrating the whole spectrum with a multi-gaussian fit using `find_peak` and `mg_fit` (Fig 2.13 and 2.14).

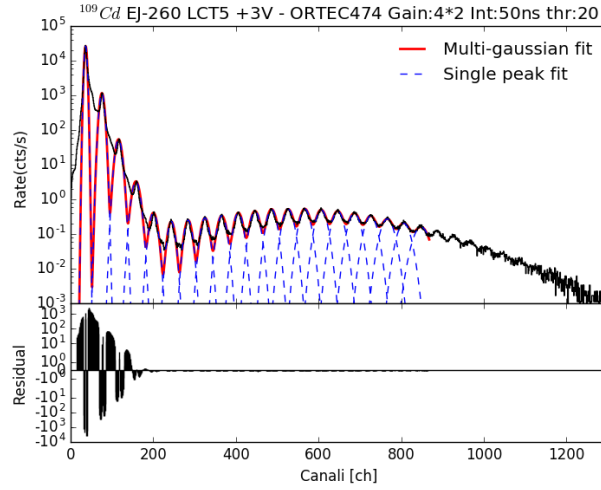


Figure 2.13: Integration of acquired spectrum of ^{109}Cd @ 22keV with EJ-260+LCT5/1 (+3V). The y-scale is Logarithmic to show the 4 orders of magnitude difference rate between dark noise and photo-peak.

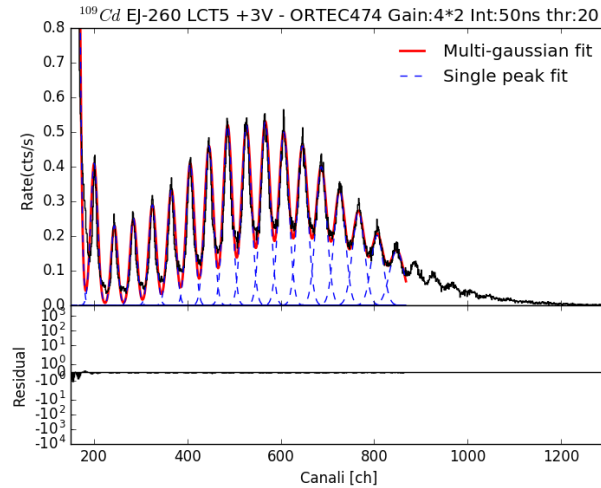


Figure 2.14: Integration of acquired spectrum of ^{109}Cd @ 22keV with EJ-260+LCT5/1 (+3V). (Linear scale)

SiPM spectrum has Poissonian distribution (discussed in ..), and therefore I expected a constant value for $FWHM/\sqrt{N}$, where FWHM is the width of single PE peaks and N is the number of considered PE. Result example of `fwhm_lin` is showed in Fig 2.15.

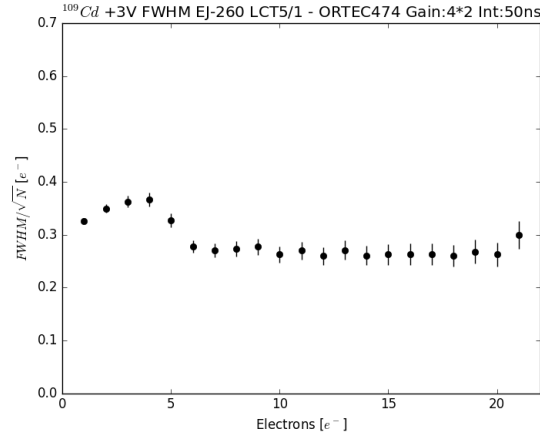


Figure 2.15: $FWHM/\sqrt{N}$. [^{109}Cd @ 22keV with EJ-260+ LCT5/1 (+3V)].

With fit parameters I was able to study all main SiPM characteristics and photo-peak information, i.e. scatterer differences.

Linearity is **well defined** because of high number of single photon detection with a good resolution ($\sim 10\%$), for this reason I calibrated ADC channels as function of photo-electrons number (Eq 2.3).

$$channel = A \cdot e^- + B \quad (2.3)$$

Function (2.3) is included in `cal_lin` task. A calibration example is showed in Fig 2.16.

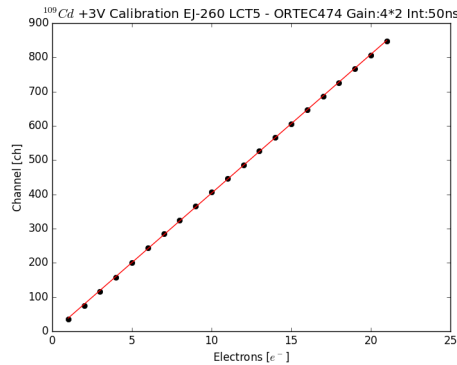


Figure 2.16: Calibration of integrated spectrum. [^{109}Cd @ 22keV with EJ-260+ LCT5/1 (+3V)].

I expected that difference between calibrated position of photon-electron peaks was $\sim 1e^-$. I considered this assumption as a further test for linearity (Fig 2.17) and for this I used `position_diff` task.

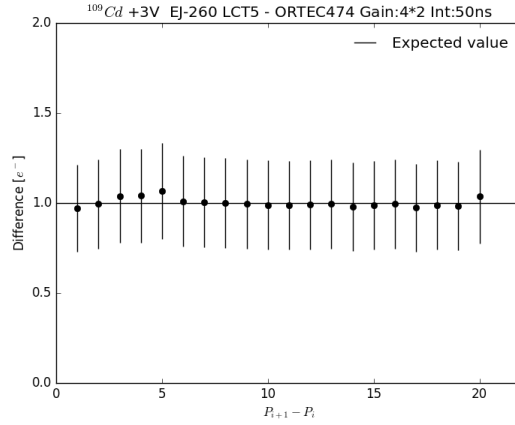


Figure 2.17: Differences between calibrated position of PE peaks. [^{109}Cd @ 22keV with EJ-260+ LCT5/1 (+3V)].

I obtained spectrum information integrating the area of single PE peaks. The resulting curve is the source photo-peak with a gaussian distribution (Fig 2.18). I fitted this curve with `fit_area` task, that is a simple gaussian fit which reads *centroid* (C) position as collected charge, *amplitude* as counting rate per second, and FWHM as resolution (R) defined by (2.4).

$$R = \frac{FWHM[e^-]}{C[e^-]} \quad (2.4)$$

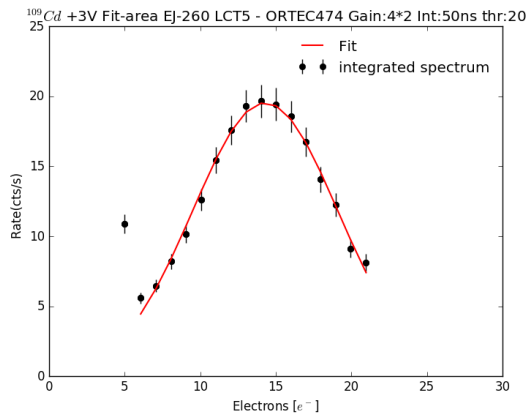


Figure 2.18: Integrated photo-peak area. [^{109}Cd @ 22keV with EJ-260+ LCT5/1 (+3V)].

First PE width and amplitude values (1 to 5 e^-) are quite inconsistent compared to high energy peaks, because of high rate that causes peak distortion and consequently a difficulty to fit curves increasing errors. Other distortions are introduced by increasing the overvoltage value, that makes totally asymmetric peaks (Fig 2.19).

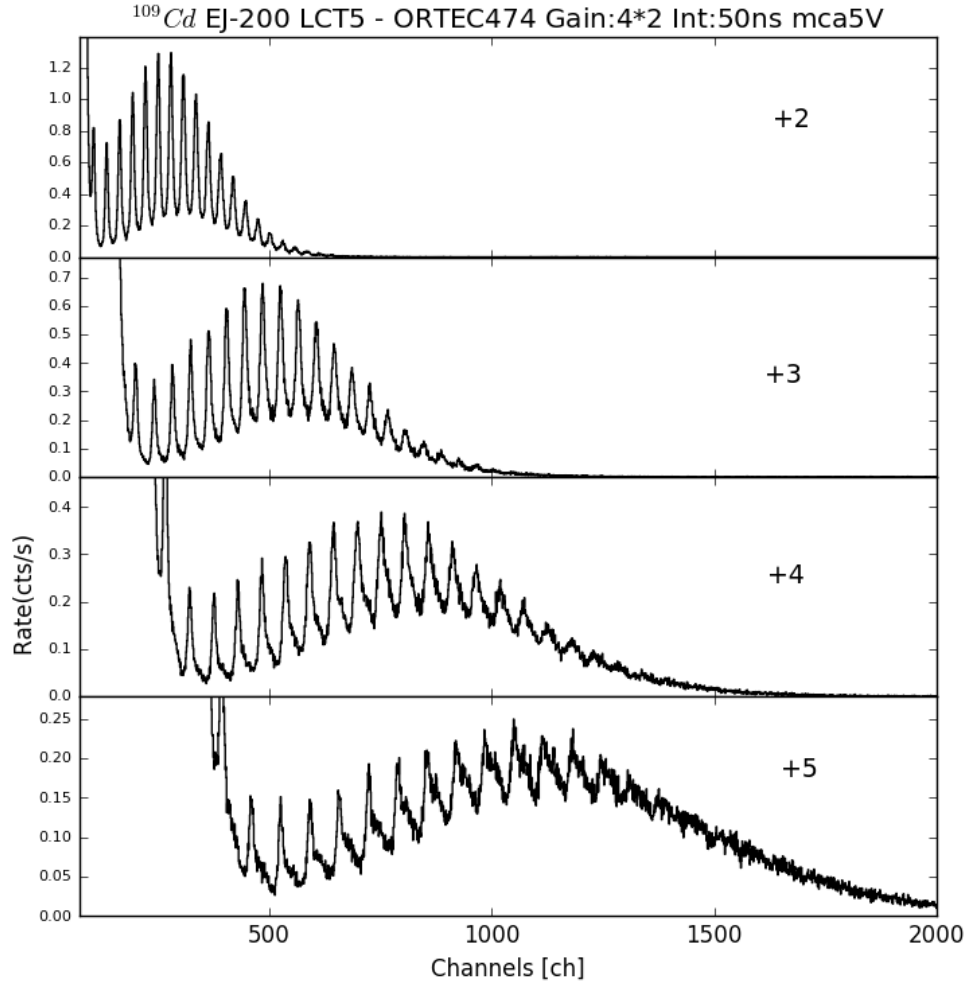


Figure 2.19: Acquired spectrum of ^{109}Cd @ 22keV with EJ-260+ LCT5/1 (+3V) while varying overvoltage.

In this case used software does not converge while fitting, therefore I calculated position and photo-peak area by **numerical integration**. This way is logically more inaccurate than analytical study, because I cannot elaborate a model that explains right distortions due to SiPM impurities and pile-up events.



I analyzed EJ-200 (Fig 2.20), EJ-204 (Fig 2.21) and EJ-260 (Fig 2.22) spectra using explained methodology. Calibration results are listed in Tab (..) and fit results in Tab 2.3.

FIT RESULTS							
Scatterer	Center [e^-]	$\sigma[e^-]$	FWHM [e^-]	Area [cts/s]	χ^2_{red}	Res [%]	V_{op} [V]
EJ-200	10.13 ± 0.02	3.86 ± 0.03	9.09 ± 0.07	248 ± 1	0.1	89 ± 6	+2
	12.8 ± 0.1	4.4 ± 0.1	10.3 ± 0.2	240 ± 5	0.86	80 ± 2	+3
	14.0 ± 0.1	4.5 ± 0.1	10.5 ± 0.2	211 ± 6	0.57	75 ± 1	+4
	17 ± 1	-	-	210 ± 18	-	-	+5
EJ-204	11.02 ± 0.05	4.22 ± 0.06	9.9 ± 0.1	253 ± 4	0.62	89 ± 1	+2
	13.81 ± 0.04	5.0 ± 0.4	11.7 ± 0.9	262 ± 3	0.29	84 ± 4	+3
	15.51 ± 0.08	5.6 ± 0.1	13.1 ± 0.2	269 ± 5	0.51	84 ± 1	+4
	20.32 ± 0.07	7.4 ± 0.1	17.4 ± 0.2	255 ± 9	0.16	85 ± 1	+6
EJ-260	11.03 ± 0.03	4.07 ± 0.03	9.58 ± 0.08	236 ± 1	0.1	86.8 ± 0.7	+2
	14.29 ± 0.06	4.79 ± 0.08	11.2 ± 0.1	234 ± 3	0.3	78.3 ± 0.7	+3

Table 2.3: Fit results for EJ-200, EJ-204 and EJ-260 while varying V_{op}

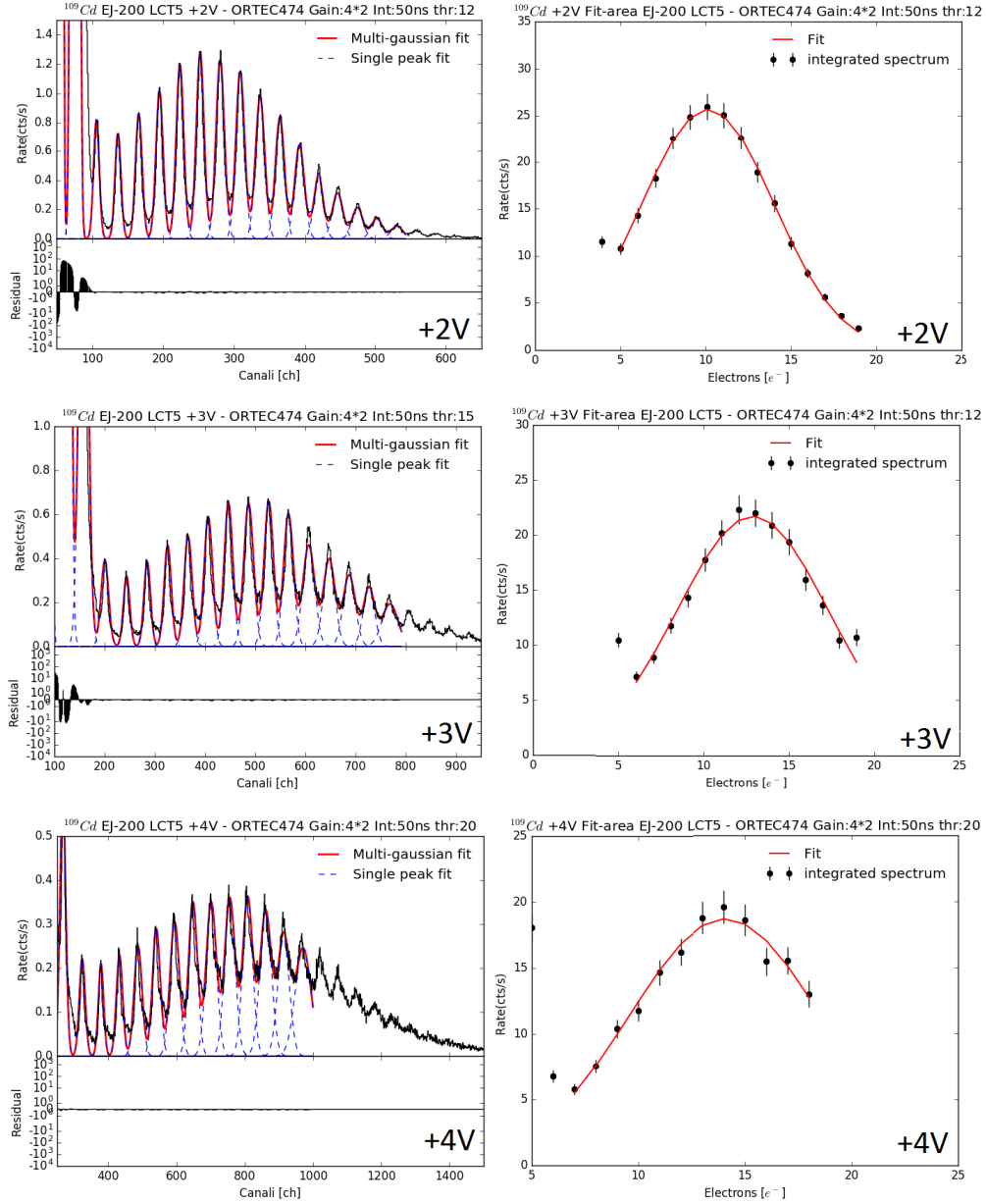


Figure 2.20: Acquired spectrum of ^{109}Cd @ 22keV with EJ-200+ LCT5/1 while varying overvoltage. Left figure: acquired spectrum. Right figure: integrated spectrum.

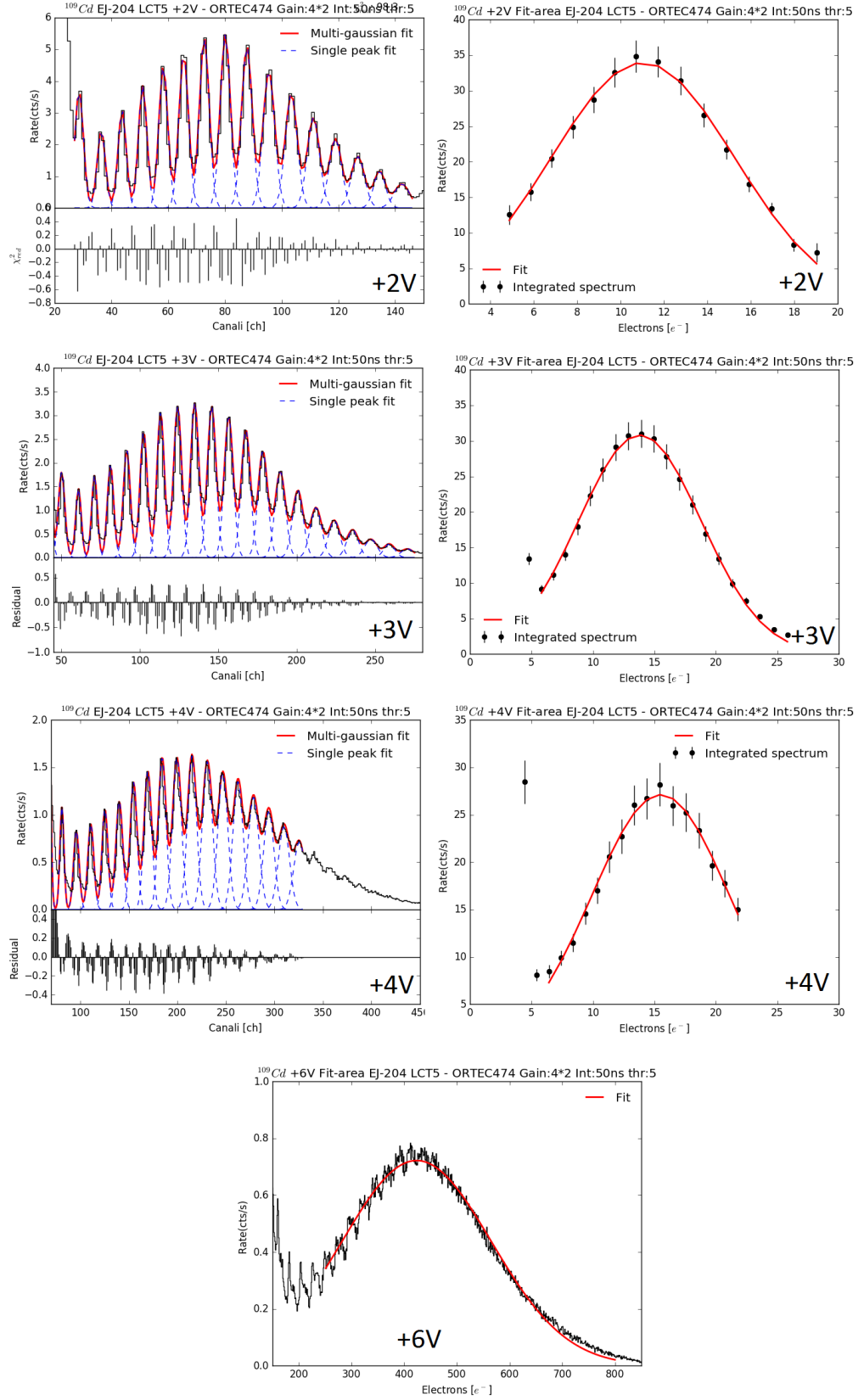


Figure 2.21: Acquired spectrum of ^{109}Cd @ 22keV with EJ-204+ LCT5/1 while varying overvoltage. Left figure: acquired spectrum. Right figure: integrated spectrum.

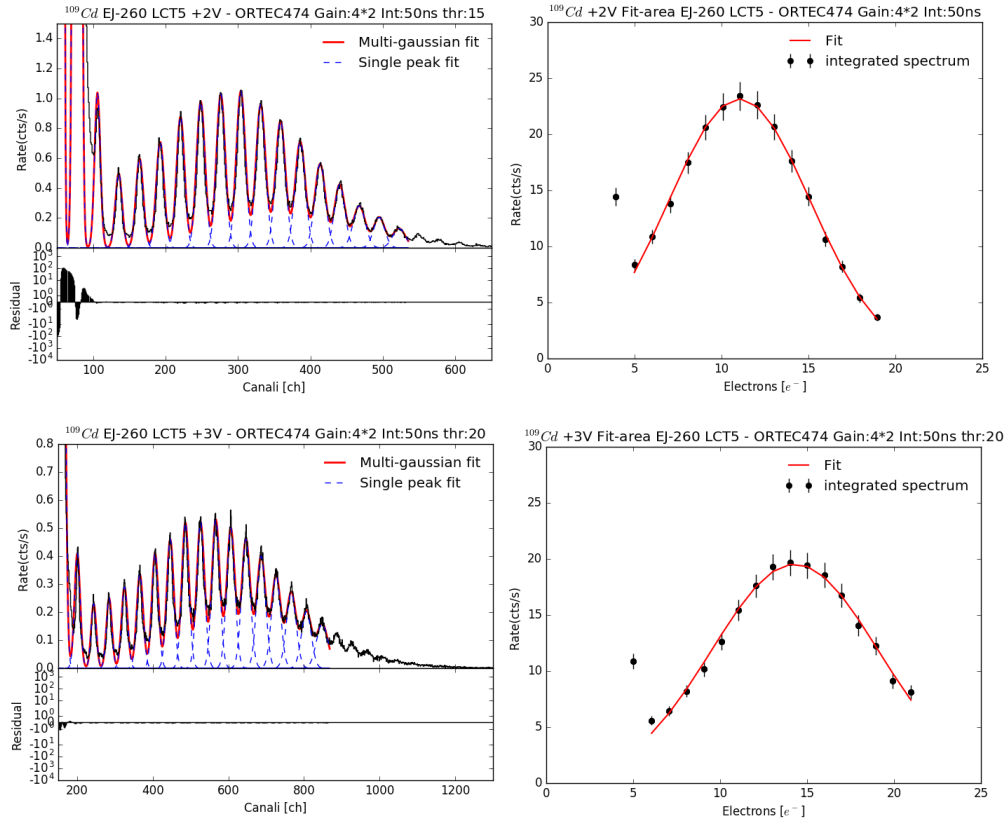


Figure 2.22: Acquired spectrum of ^{109}Cd @ 22keV with EJ-260+ LCT5/1 while varying overvoltage. Left figure: acquired spectrum. Right figure: integrated spectrum.

Bibliography

- [1] Hye-Lim Kim et al. Journal of Ceramic Processing Research. Vol. 16, No. 1, pp. 124-128, 2015
- [2] Ce:GAGG Scintillator Crystal, datasheet from Furukawa website (<http://www.furukawa-denshi.co.jp/cgi-bin/pdfdata/20140428162950.pdf>)
- [3] XCOM: Photon Cross Sections Database <http://www.nist.gov/pml/data/xcom/>
- [4] Section Gamma and X-Ray Standards. http://www.ezag.com/fileadmin/ezag/user-uploads/isotopes/isotopes/Isotrak/isotrak-pdf/Product_literature/EZIPL/Gamma_Standards_All_Types.pdf
- [5] Bonanno et al. doi:10.1016/j.nima.2015.10.064
- [6] Seferis et al. doi:10.1007/978-3-319-00846-2-113, 2013
- [7] General purpose plastic scintillator, EJ-200, EJ-204, EJ-208, EJ-212. http://www.eljentechnology.com/images/products/data_sheets/EJ-200_EJ-204_EJ-208_EJ-212.pdf
- [8] Green emitting plastic scintillator, EJ-260, Ej-262. http://www.eljentechnology.com/images/products/data_sheets/EJ-260_EJ-262.pdf
- [9] EJ-200 plastic scintillator. <http://www.ggg-tech.co.jp/maker/eljen/ej-200.html>
- [10] EJ-204 plastic scintillator. <http://www.ggg-tech.co.jp/maker/eljen/ej-200.html>
- [11] EJ-260 plastic scintillator. <http://www.ggg-tech.co.jp/maker/eljen/ej-260.htm4>
- [12] Bonanno et al., NIM A, 806, 383, 2016